Supplementary Information (SI) for Materials Chemistry Frontiers.
This journal is © the Partner Organisations 2026

Supplementary Information (SI) for Materials Chemistry Frontiers.
This journal is © the Partner Organisations 2025

Supporting Information

A Weavable DC Triboelectric Nanogenerator Fiber Driven by Dynamic Electric Double Layers

Kuo Li,[†a] Ning Wang,[†a] Zhouquan Sun,[a] Kerui Li,[a] Yaogang Li,[a] Qinghong Zhang,[a], Hongzhi Wang*[a, b], Chengyi Hou*[a]

a.State Key Laboratory for Advanced Fiber Materials, College of Materials Science and Engineering, Donghua University, Shanghai 201620, P. R. China..

b.School of Materials Science and Engineering, Shanghai Dianji University, Shanghai 201306, P. R. China.

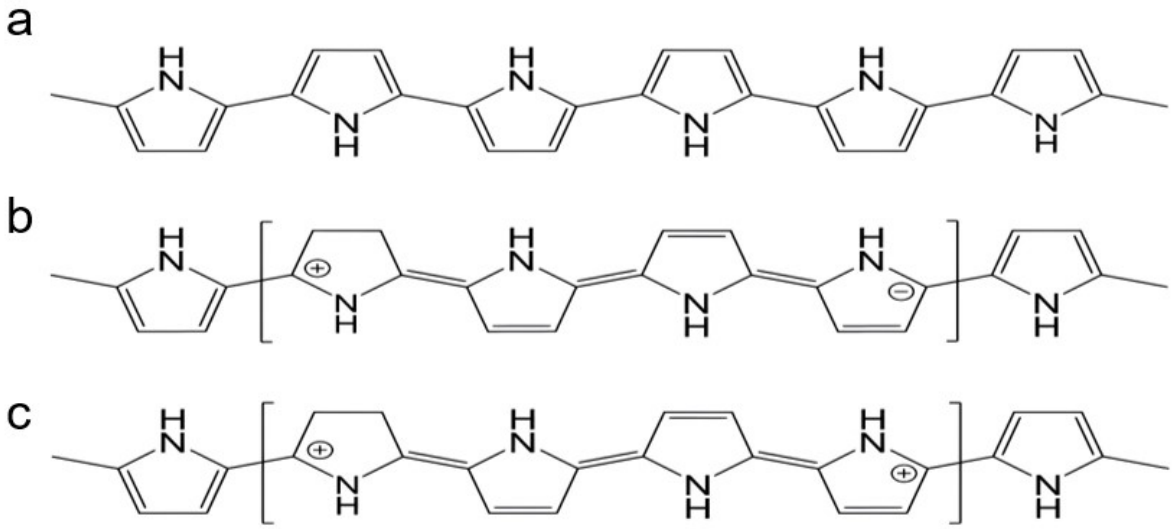

Fig. S1 Molecular structure of PPy (a) neutral, (b) polaron and (c) bipolaron.

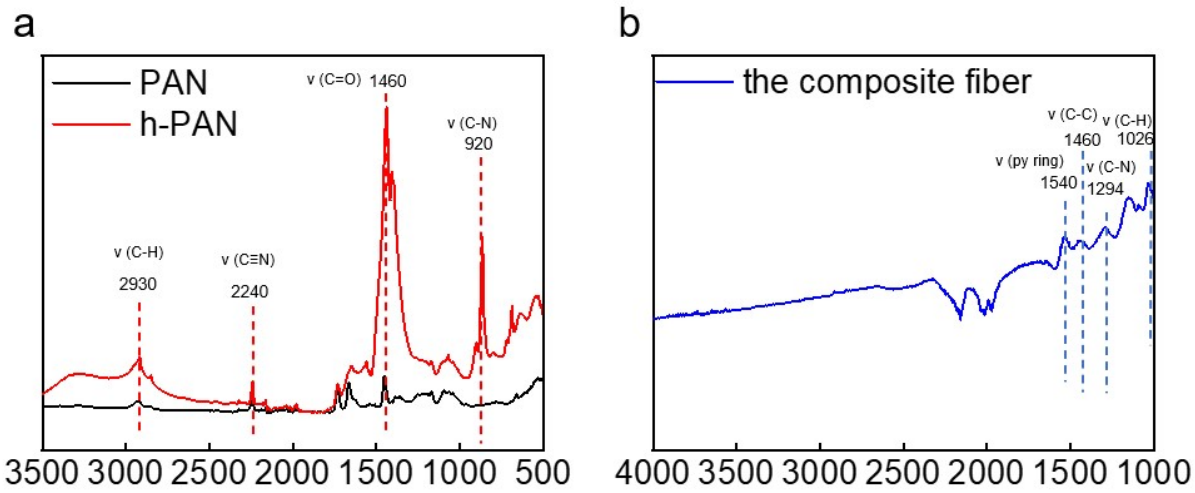

Fig. S2 The comparative FTIR spectrumof Fibers Before and After PPY Coating.

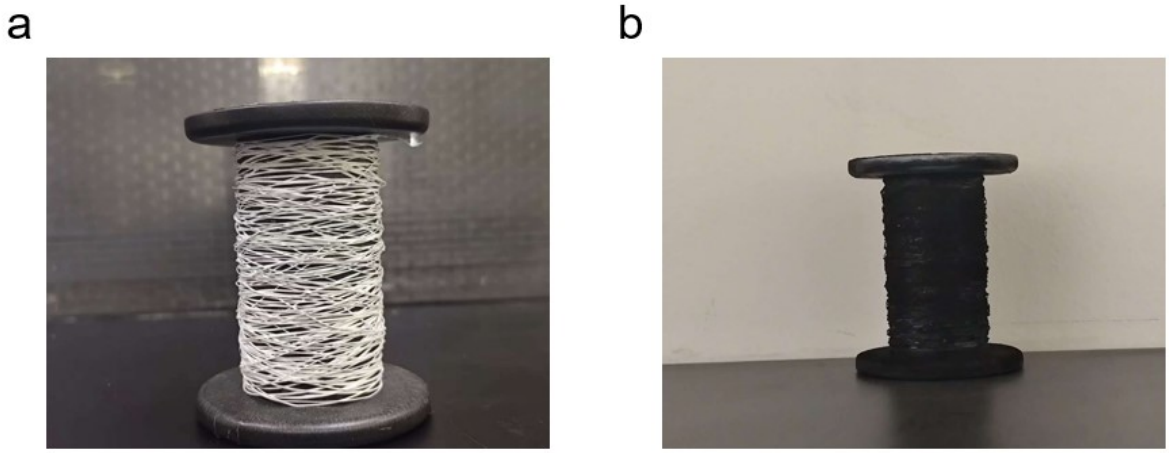

Fig. S3 Continuous fabrication of fibers: (a) PAN nanofibers; (b) the composite fiber.

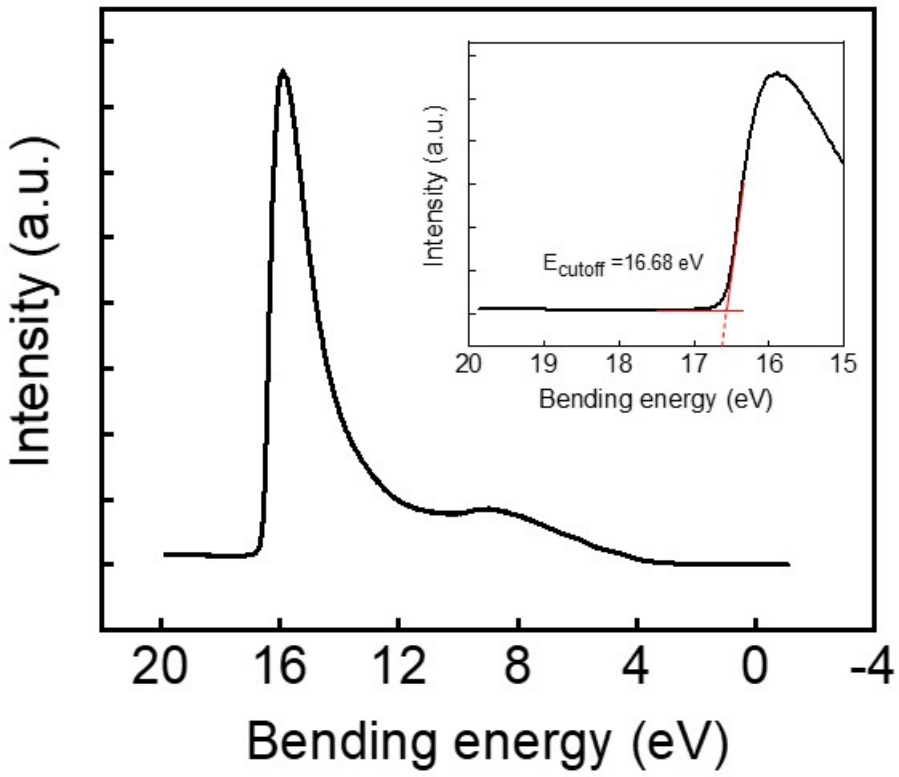

Fig. S4 Work function of the composite fiber. Ultraviolet photoelectron spectroscopy (UPS) with an excitation energy of He I (21.2 eV) was employed to characterize the electronic structure of the PPy. The work function of the material surface can be determined using WF = hv - Ecutoff. Thus, the work function

measured from these spectra for the PPy is 4.52 eV.

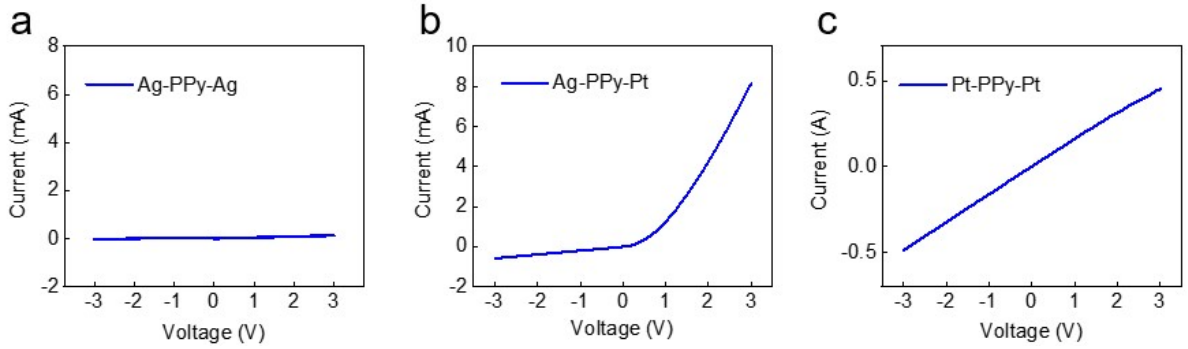

Fig. S5 I-V curves for (a) Ag-PPy-Ag, (b) Ag-PPy-Pt, and (c) Pt-PPy-Pt.

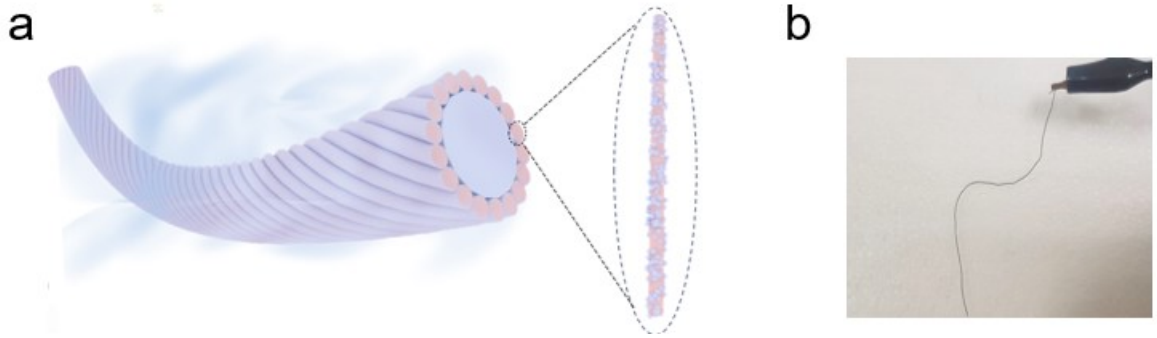

Fig. S6 Morphology of the composite fiber. (a) Side-view and (b) photograph of the as-prepared fibers.

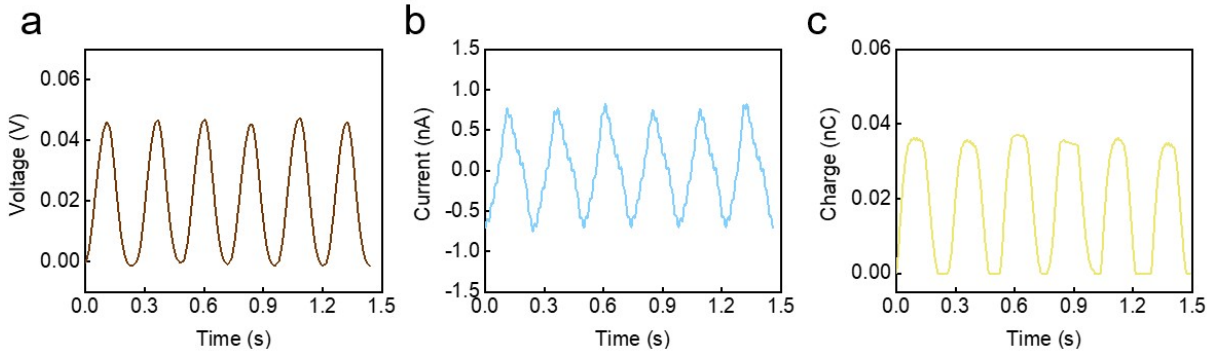

Fig. S7 Typical output of the generator in proximity-separation mode under 100% humidity: (a) voltage, (b) current, and (c) transferred charge.

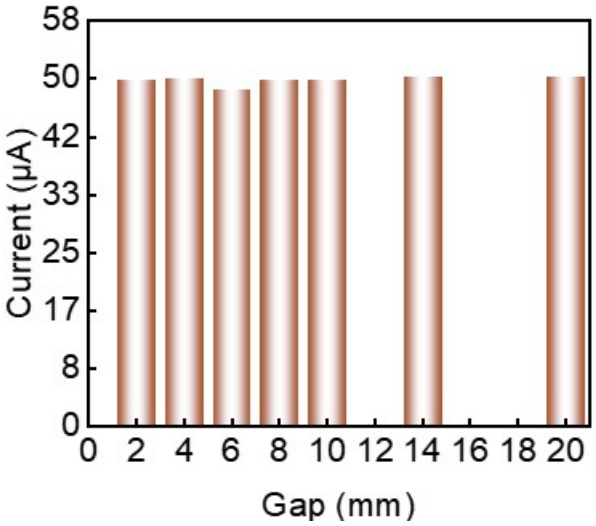

Fig. S8 Short-circuit current of generator under contact-disconnect mode at 100% humidity for different disconnecting gaps

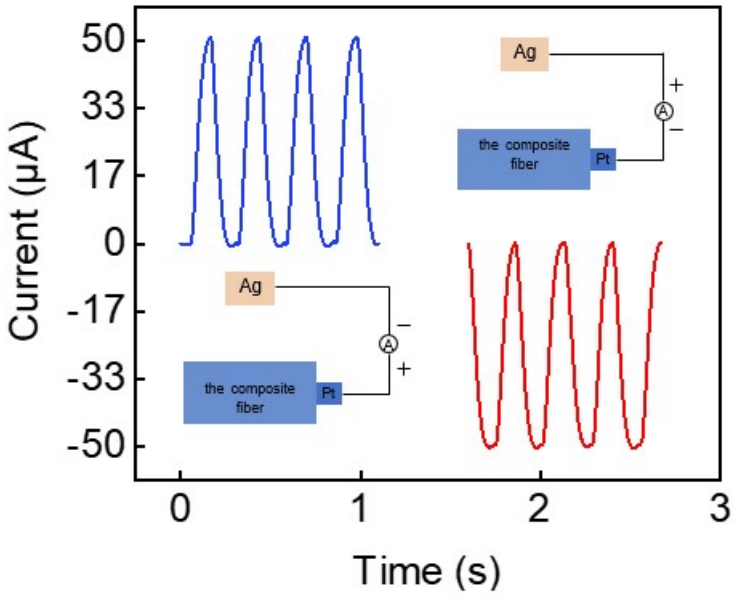

Fig. S9 Reverse connection of external measurement at 100% humidity. Current reverses when circuit connections are altered. The blue and red curves represent short-circuit currents when the device is connected to the voltmeter in forward and reverse directions, respectively.

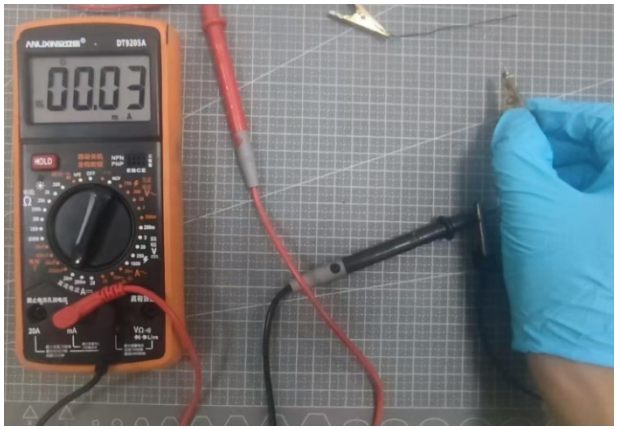

Fig. S10 Experimental verification of charge polarity by measuring transient current with a digital multimeter.

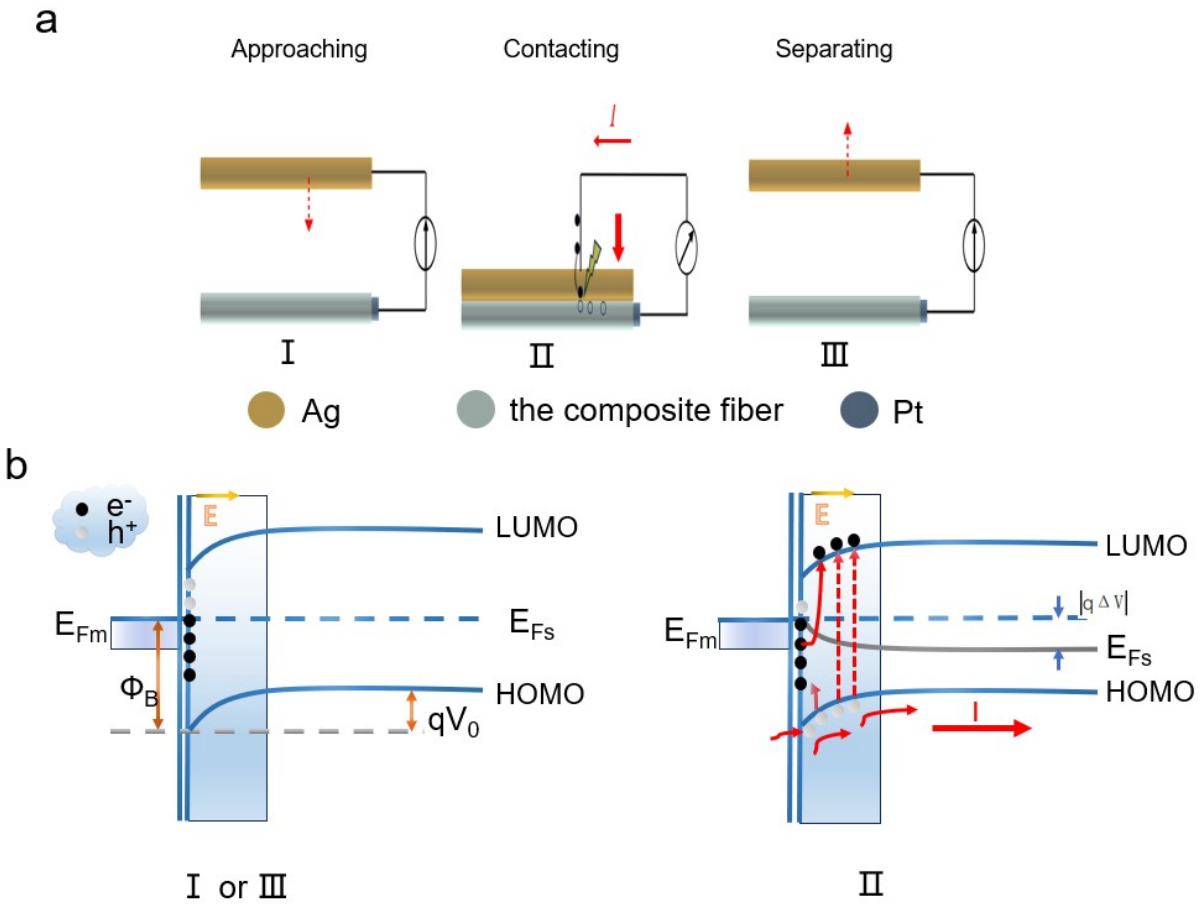

Fig. S11 Mechanism of the DC-TEF. Schematic illustration of the power generation mechanism under contact–separation between Ag wire and in-situ polymerized PPy on non-hydrolyzed PAN nanofibers.

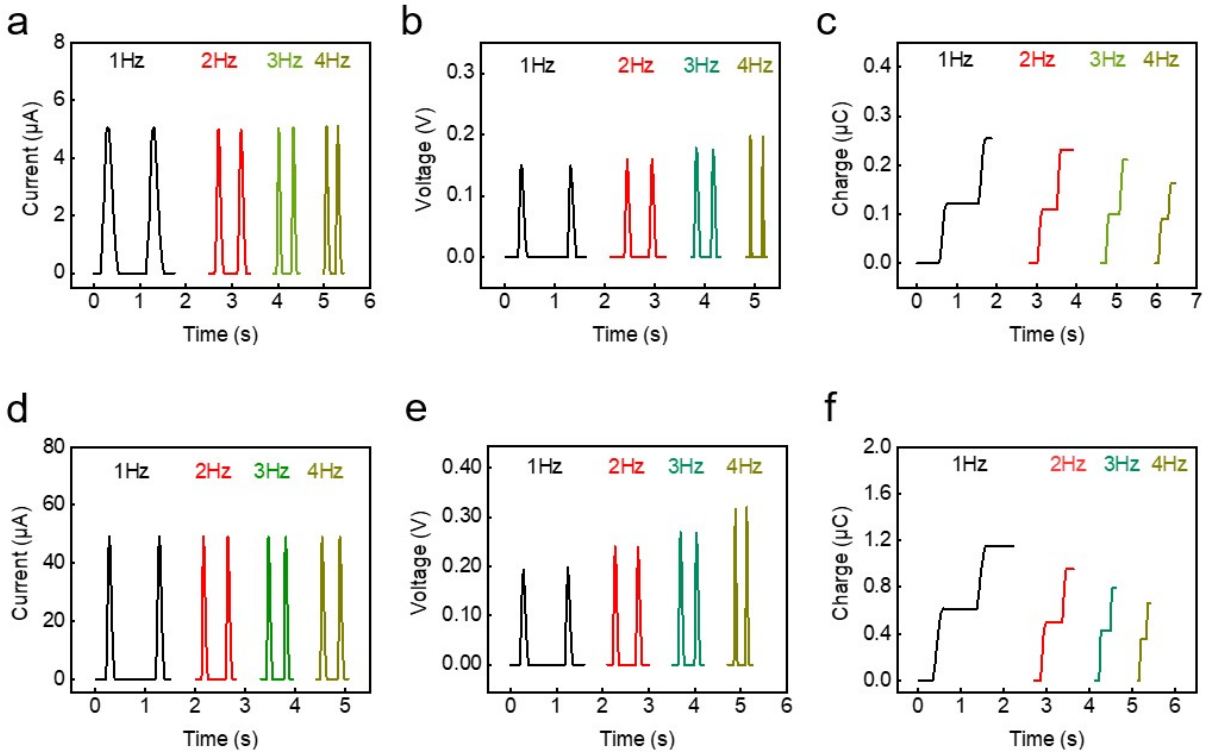

Fig. S12 Output performance versus operating frequency of the two fiber types before and after hydrolysis at 100% humidity: (a)-(c) current, voltage, and transferred charge of the DC-TENG; (d)-(f) current, voltage, and transferred charge of the SDC-TENG.

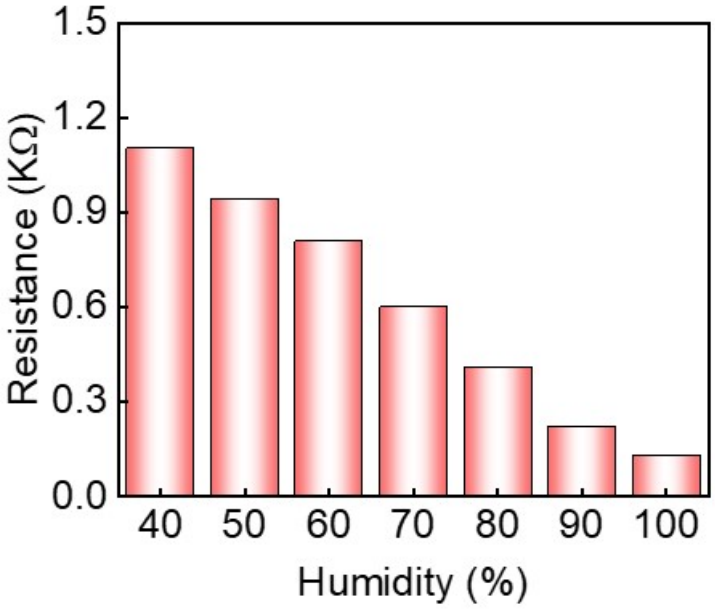

Fig. S13 Surface resistance of the composite fiber as a function of humidity: the resistance decreases with increasing humidity.

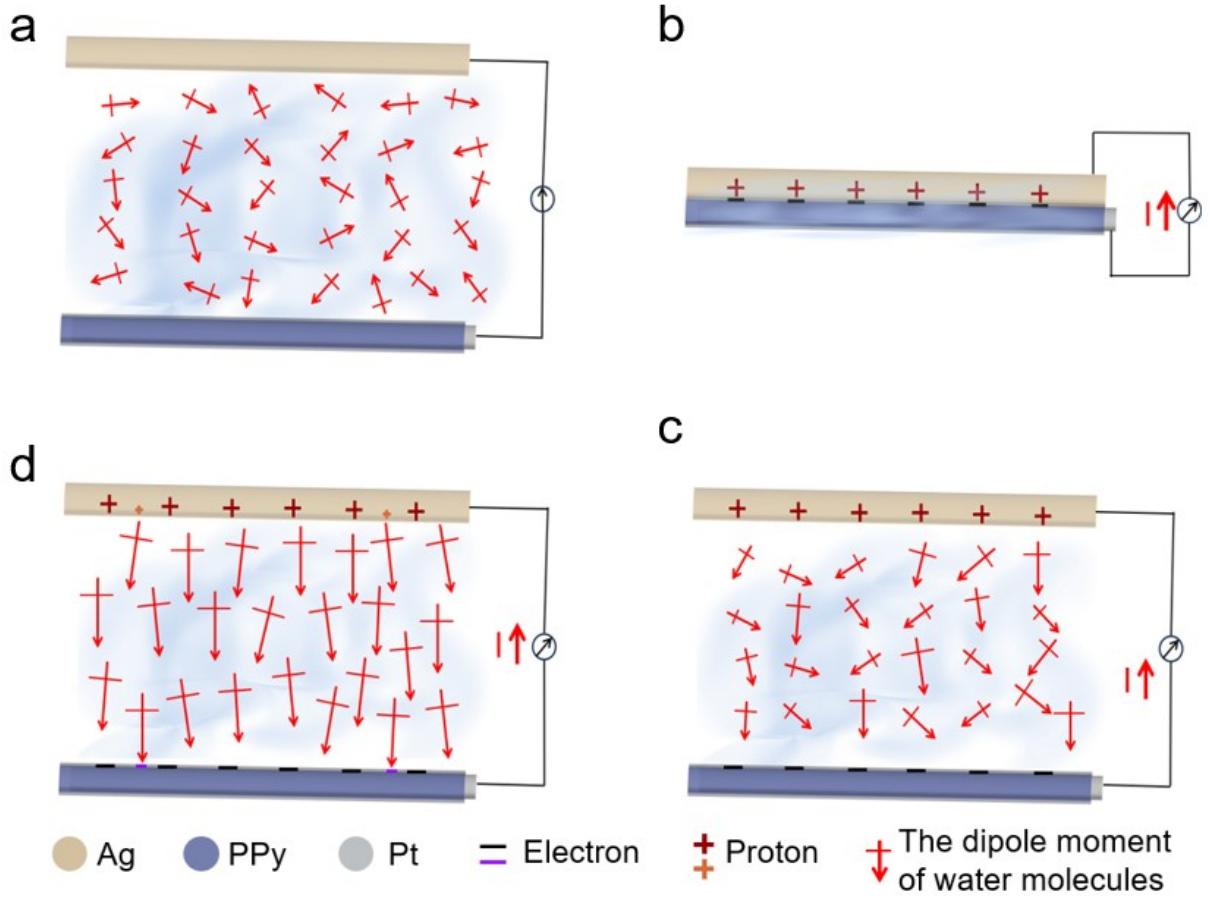

Fig. S14 Impact of distilled water molecules on the HWF mechanism. Replacing ambient water molecules with distilled ones shows that distilled water can also polarize and promote additional charge generation.

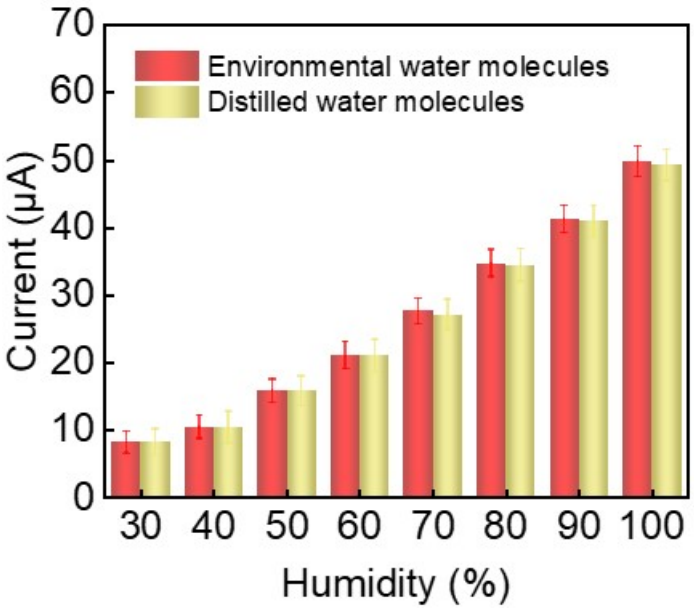

Fig. S15 Comparison of output current: ambient vs. distilled water molecules. This Fig. compares the output currents of the HWF when ambient water molecules are replaced with distilled water molecules.

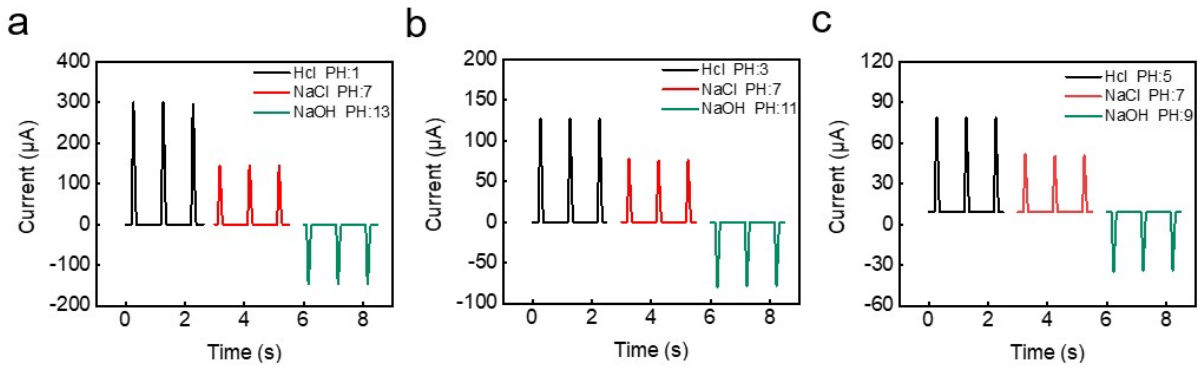

Fig. S16 Influence of ion concentration on output current at 75% humidity. (a)-(c) Output currents at HCl,

NaCl, and NaOH concentrations of 0.1 M, 0.001 M, and 0.00001 M, respectively

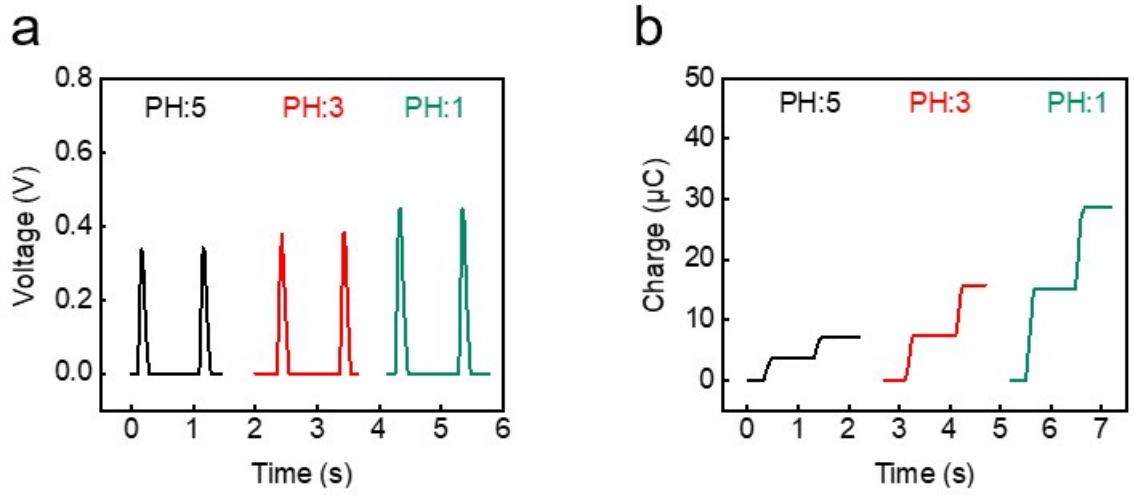

Fig. S17 Effect of H^+ concentration on voltage and transferred charge at 75% humidity. (a) Voltage increases with increasing proton concentration. (b) Transferred charge increases with increasing proton concentration.

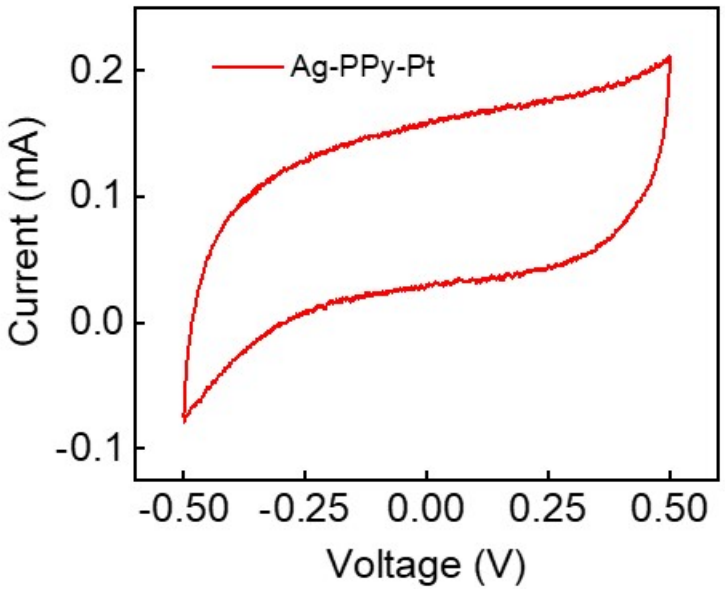

Fig. S18 Cyclic voltammetry (CV) curves of the Ag–PPy–Pt.

Fig. S19 Optical image of electrospun PAN nanofibers.

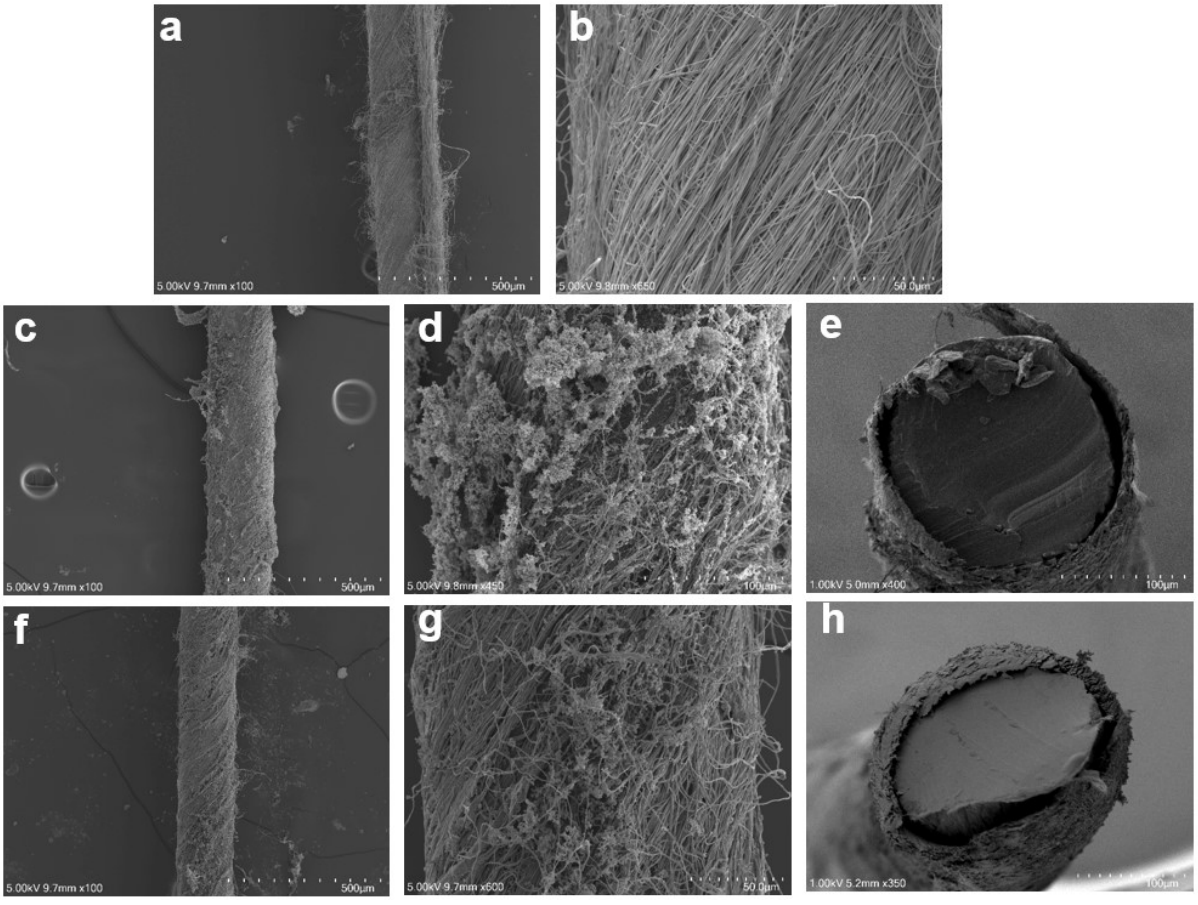

Fig. S20 SEM images: (a)-(b) surface morphology of PAN nanofibers; (c)-(e) surface and cross-sectional views of the composite fiber before hydrolysis; (f)-(h) surface and cross-sectional views of the composite fiber after hydrolysis.

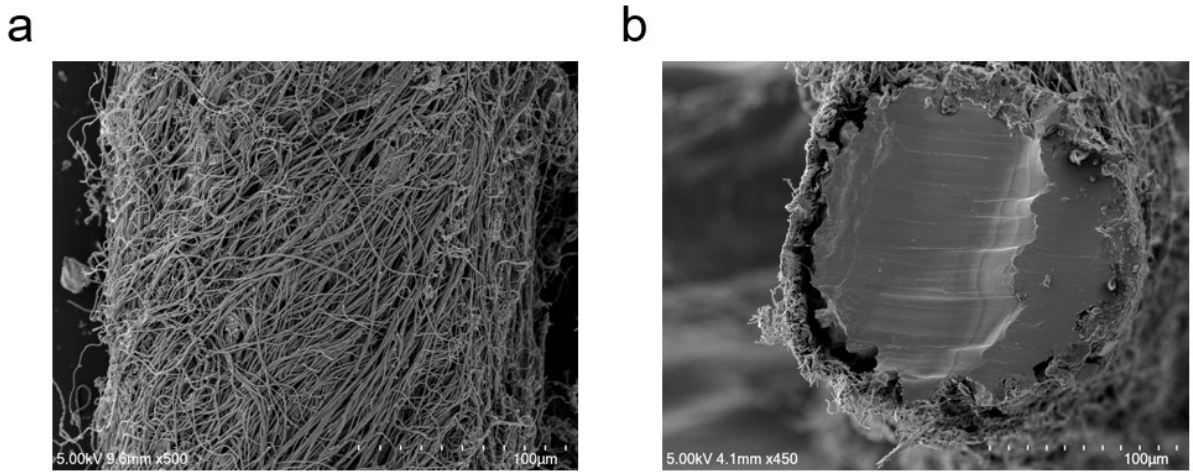

Fig. S21 SEM images of the HWF after 20,000 cycles: surface and cross-sectional views.

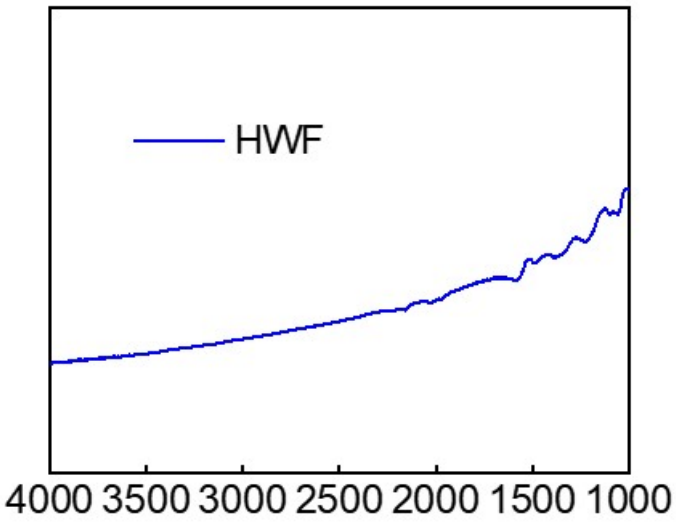

Fig. S22 FTIR spectra of HWF after 20,000 cycles.

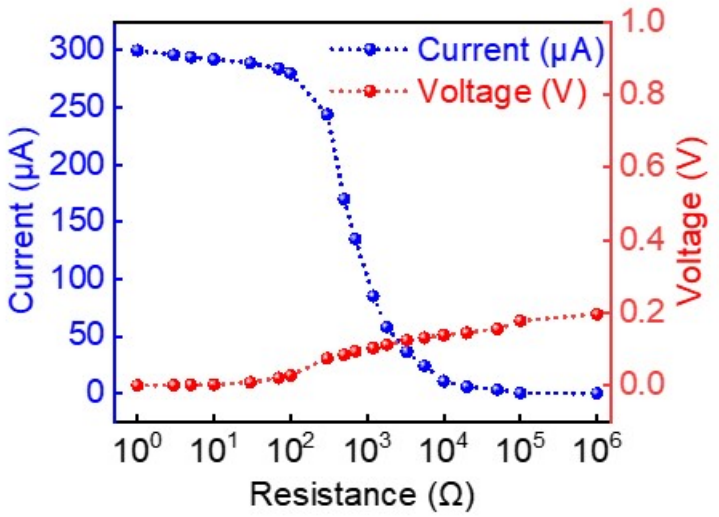

Fig. S23 Output voltage and current of the HWF as functions of load resistance.

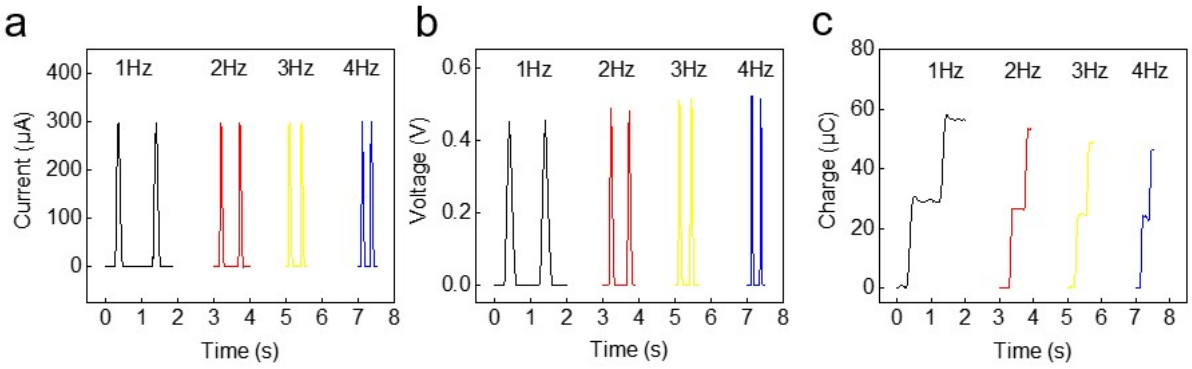

Fig. S24 Influence of operating frequency on the output performance of the HWF at 75% relative humidity: (a) current, (b) voltage, (c) transferred charge.

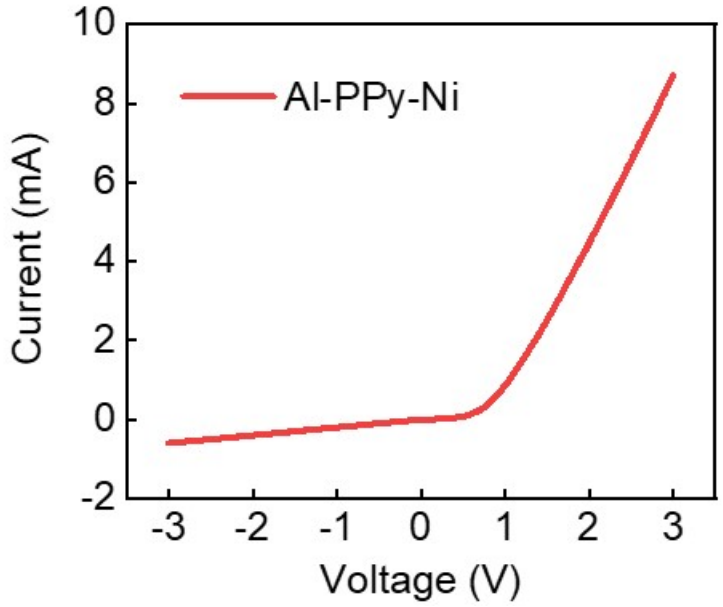

Fig. S25 Current–voltage (I–V) characteristic curves of the Al–PPy–Ni.

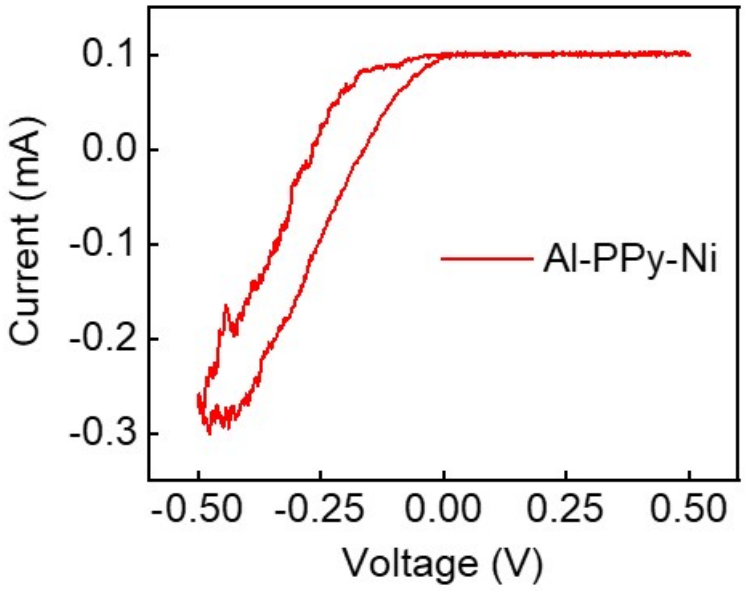

Fig. S26 Cyclic voltammetry (CV) curves of the Al–PPy–Ni.

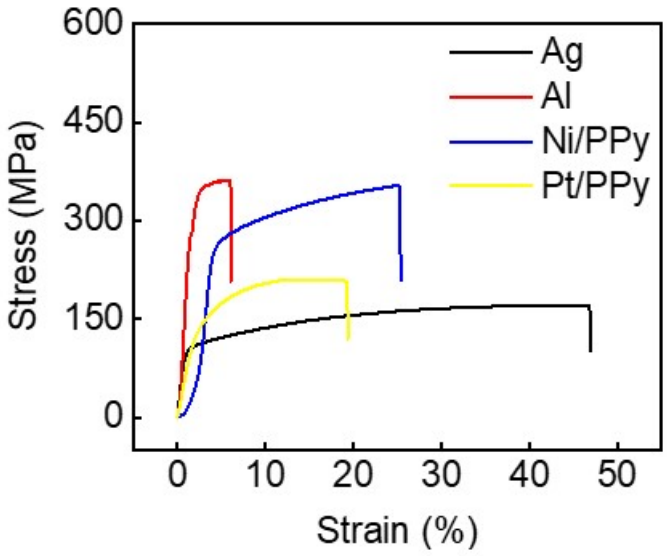

Fig. S27 Tensile strength of the four fibres in the experiment.

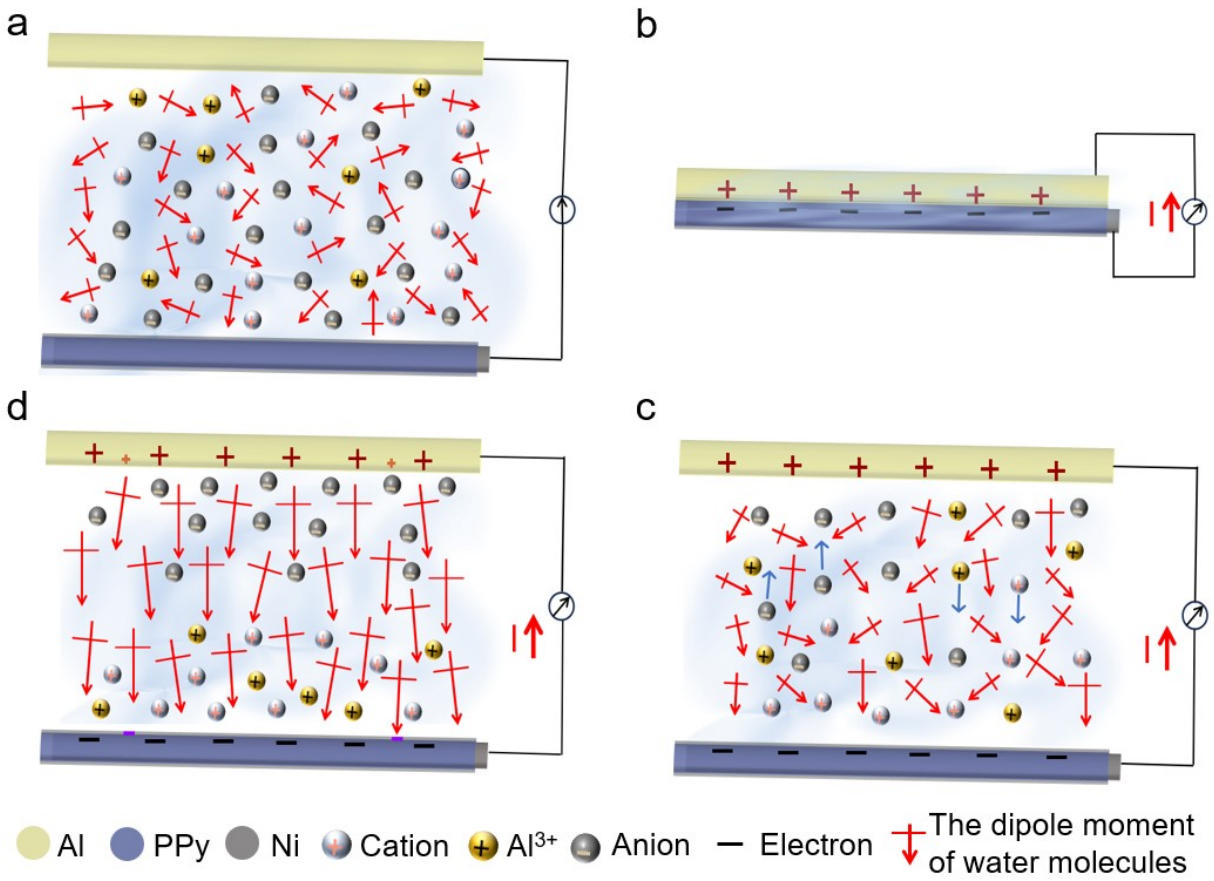

Fig. S28 Working principle of the optimized HWF. (a) Dispersed water molecules between the aluminum wire and the composite fiber before contact. (b) Upon contact, electrostatic interaction induces positive charges on the Al surface and negative charges on the composite surface. (c) Polarization of interfacial

water molecules drives directional ion migration, forming two asymmetric electric double layers. (d) The sustained polarization of water molecules promotes enhanced charge generation and continues to drive ion migration until the electric double layers reach dynamic equilibrium.

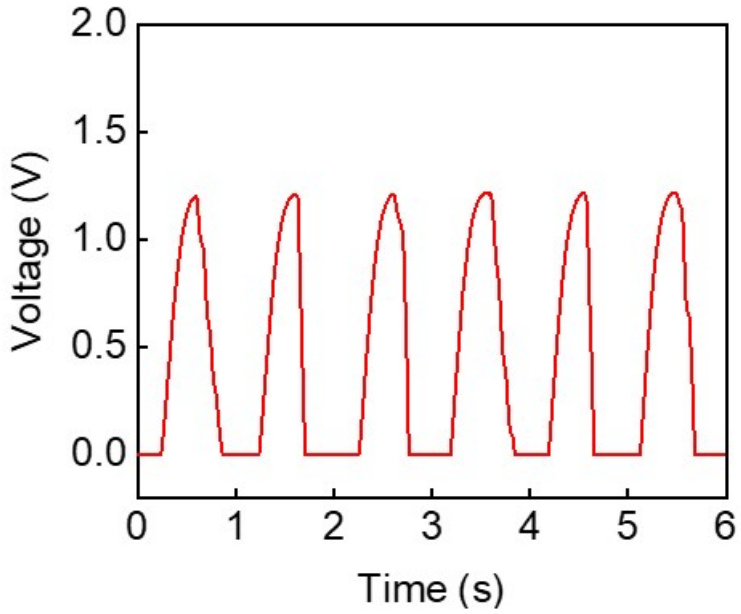

Fig. S29 Operating voltage of the Optimized HWF. The device achieves a voltage of 1.22 V at 75% relative humidity.

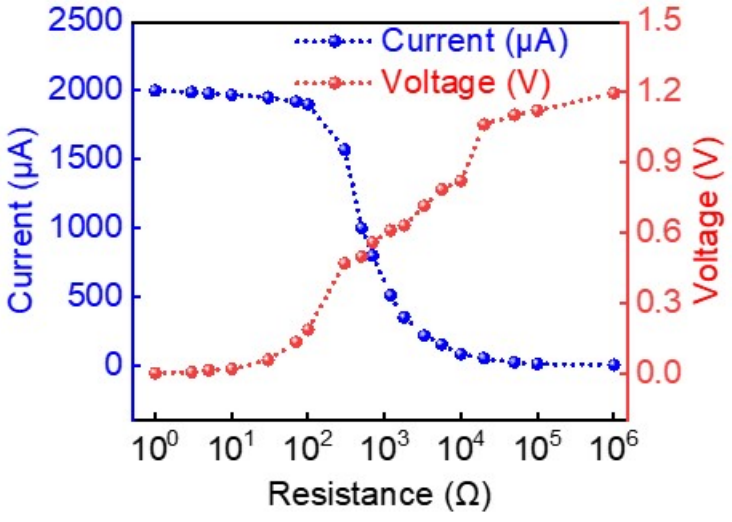

Fig. S30 Output voltage and current of the Optimized HWF as functions of load resistance.

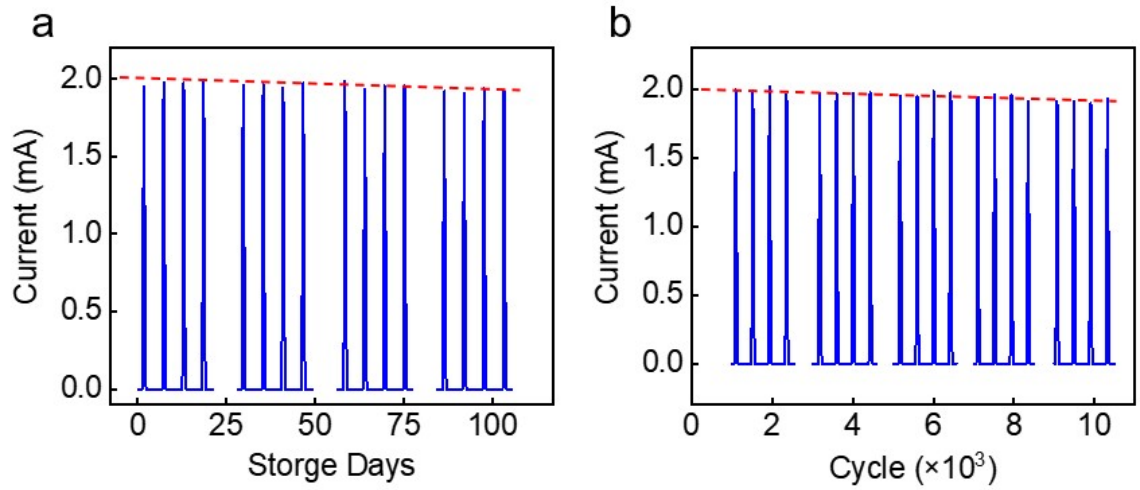

Fig. S31 Environmental Stability (a) Optimized HWF current during 100-day intermittent testing. (b) Optimized HWF current during 10,000-cycle testing.

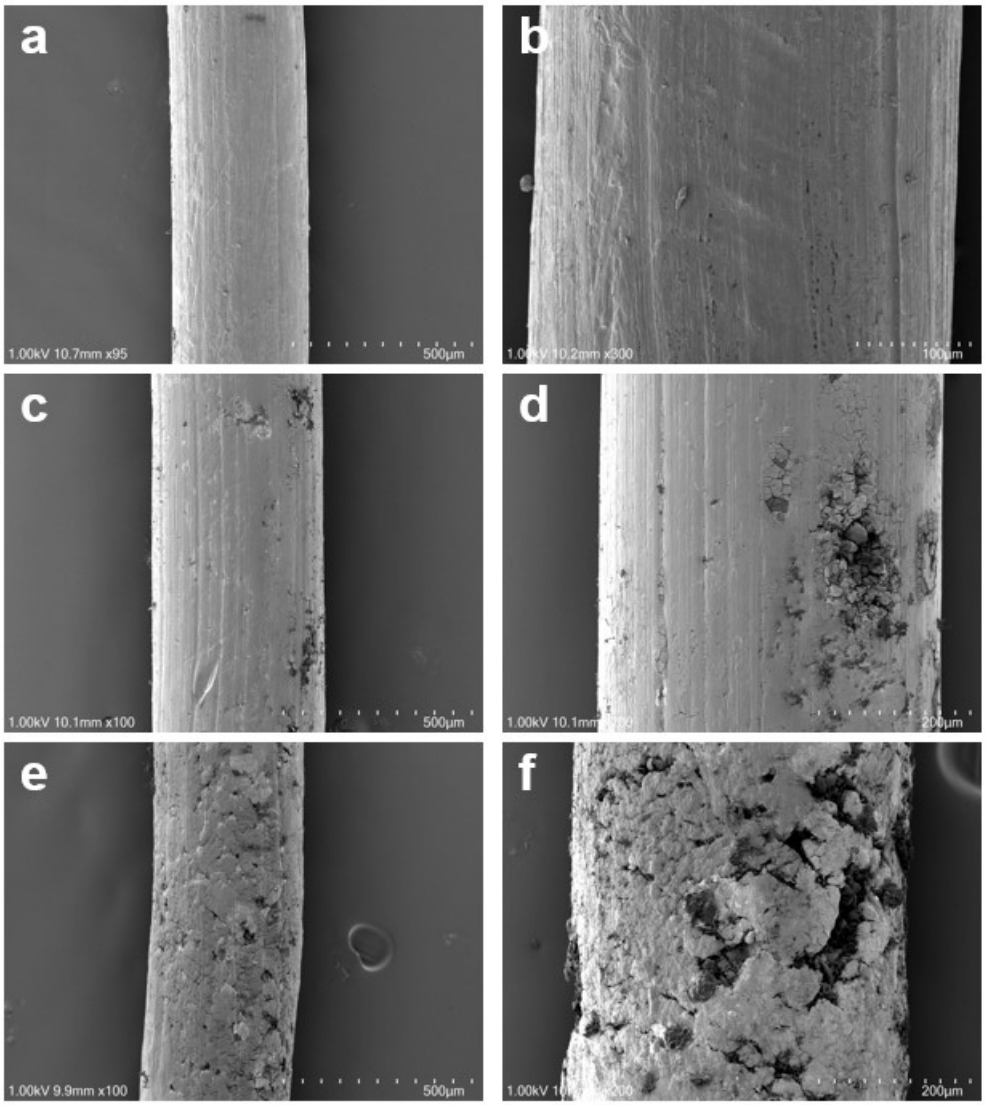

Fig. S32 SEM images. (a)-(b) Surface morphology of aluminum electrodes prior to any testing. (c)-(d) Surface morphology of aluminum electrodes after 100 days of intermittent testing at 75% humidity. (e)-(f) Surface morphology of aluminum electrodes after 100 days of intermittent testing in 0.01 M sodium chloride solution.

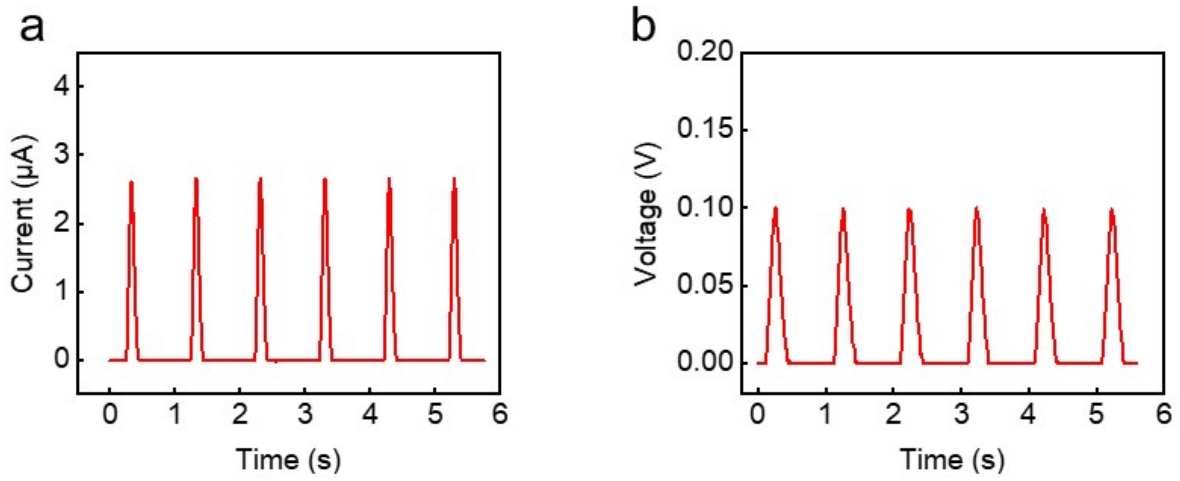

Fig. S33 Output performance of Al-PPy-Ni devices with unhydrolyzed PAN nanofibers under moisture-isolated conditions.

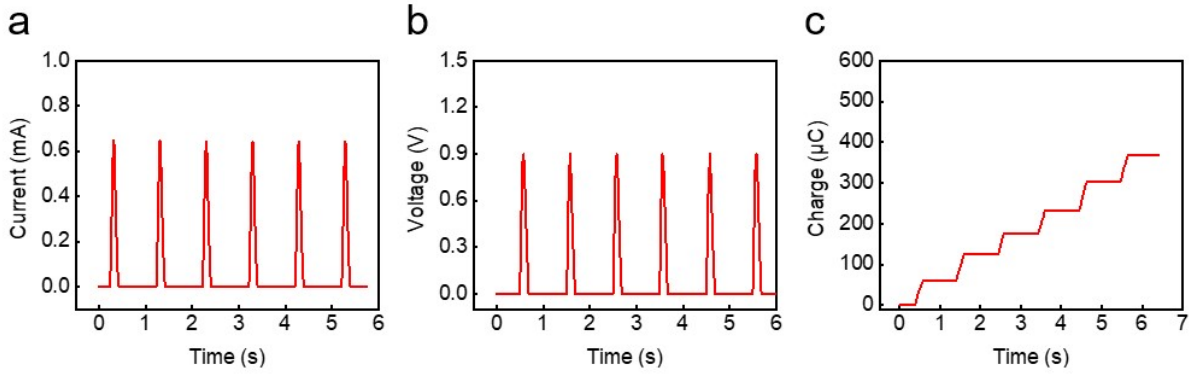

Fig. S34 Performance output from redox reactions only at 75% humidity: (a) current, (b) voltage, (c) transferred charge.

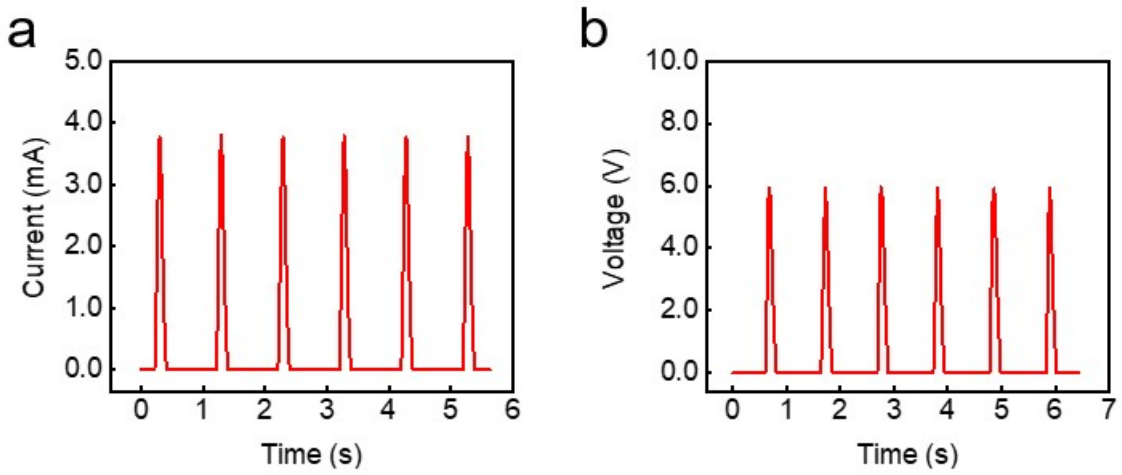

Fig. S35 Performance output of the textile at 75% humidity: (a) output current up to 4 mA, (b) output voltage up to 6 V.

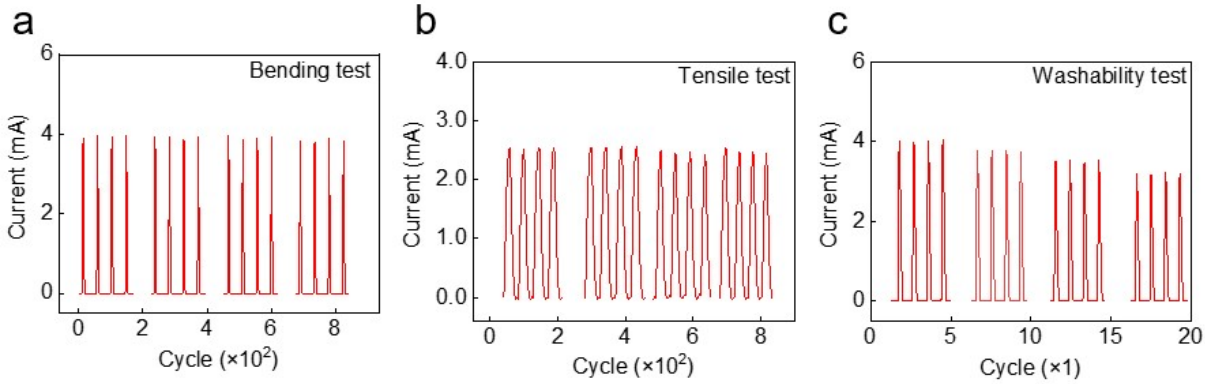

Fig. S36 Cyclic testing of fabrics under (a) bending, (b) tensile loading and (c) Washability test.

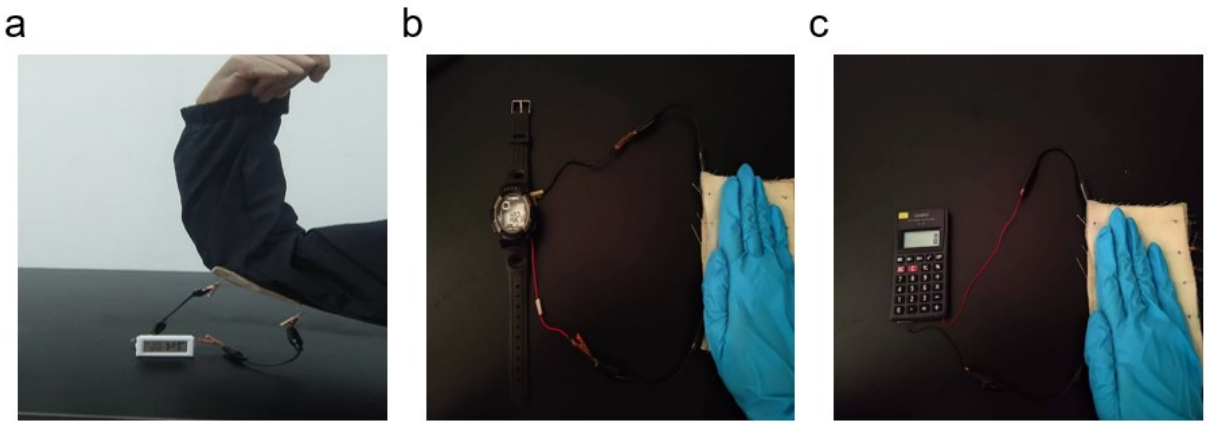

Fig. S37 Fabric drives (a) thermometers, (b) mechanical watches, and (c) calculators at 75% relative humidity.

Supporting Tables

Table S1 The performance of different types of TENGs

Material	DC-TEF	Power density (W/m^2)	Ref.
n-Si/Stainless Steel	×	0.00014	[2]
PVDF/Al	×	0.0005	[3]
Al/PEDOT:PSS	×	0.0012	[4]
Steel Ball / N-type Si Wafer	×	0.0037	[5]
n-SWCNT/ p-SWCNT	×	0.0455	[6]
PANI/Al	×	0.0731	[7]
PAA/CMFs-DESs	×	0.13	[8]
Au/PPy	×	0.15	[9]
Al/PPy	×	0.17	[10]
CsFAMA/PEDOT:PSS	×	0.18	[11]
Rotary FEP/Polyester-Fur	×	0.38593	[12]
PTFE/PU-Cu	×	0.398	[13]
PBFD/PEDOT:PF	×	1.05	[14]
Al/FEP	×	2.03	[15]
Metal-dielectric	×	2.32	[16]
DLC/Steel	×	5.815	[17]
BNPC@Elastomer/Conductive Fabric	×	6.32	[18]
CL-PTFE/SBR/BMF	×	10.6	[19]
GaN/Bi2Te3	×	11.85	[20]
PA/PET/PTFE	×	12.3	[21]
Al/PPy/Ni	√	**73.6**	This work

Table S2 Comparative Summary

Device/Mechanism	Material Design	Working Principle	Output Performance	Stability	Core Innovation
Conventional TENG	Dielectric-dielectric or dielectric-metal	Contact electrification + electrostatic induction	AC output, high voltage, low current	Excellent in dry conditions	First demonstration of mechanical energy harvesting via triboelectrification
Triboiontronic DC-TING[1-2]	Dielectric-liquid interface with pre-charged water mist	EDL regulation via contact electrification; ionic current couples with displacement current	126.40 W/m² peak power density at 0.10 Hz	Requires continuous mist supply	Dynamic EDL regulation by CE; first DC-TING based on ionic current
Our optimiezd HWF	Core-sheath fiber (Ni/Pt + hydrolyzed PAN + PPy) with Ag or Al counter electrode	ribovoltaic-driven (Schottky junction) with humidity-enhanced EDL amplification	2 mA, 1.2 V (Al-PPy-Ni); 73.6 W/m² power density	>10,000 cycles (<5% decay); 100 days intermittent	First demonstration of surface chemistry-controlled EDL amplification of tribovoltaic effect in a weavable fiber

Supplementary References

[1] Brédas, Jean-Luc, B. Themans, and J. M. Andre. "Bipolarons in polypyrrole chains." Physical Review B 27.12 (1983): 7827.

[2] Zhang, Zhi, et al. "Tribovoltaic effect on metal–semiconductor interface for direct-current low-impedance triboelectric nanogenerators." Advanced Energy Materials 10.9 (2020): 1903713.

[3] Mariappan, Vimal Kumar, et al. "Decoupling contact and rotary triboelectrification vs materials property: toward understanding the origin of direct-current generation in TENG." ACS Applied Materials & Interfaces 14.30 (2022): 34593-34602.

[4] Meng, Jia, et al. "Flexible textile direct-current generator based on the tribovoltaic effect at dynamic metal-semiconducting polymer interfaces." ACS Energy Letters 6.7 (2021): 2442-2450.

[5] Yang, Di, et al. "Tribological-behaviour-controlled direct-current triboelectric nanogenerator based on the tribovoltaic effect under high contact pressure." Nano Energy 99 (2022): 107370.

[6] Lv, Tianmei, et al. "All-Fabric Direct-Current Triboelectric Nanogenerators Based on the Tribovoltaic Effect as Power Textiles." Advanced Energy Materials 13.29 (2023): 2301178.

[7] Han, Xing, et al. "Amplifying electrical outputs of polyaniline-based Schottky DC generators through single polarity charge injection." Nano Energy 119 (2024): 109048.

[8] Yang, Ruizhe, et al. "High-performance flexible Schottky DC generator via metal/conducting polymer sliding contacts." Advanced Functional Materials 31.43 (2021): 2103132.

[9] Shao, Hao, et al. "Polymer–metal Schottky contact with direct-current outputs." Advanced Materials 28.7 (2016): 1461-1466.

[10] Meng, Jia, et al. "Durable flexible direct current generation through the tribovoltaic effect in contact-separation mode." Energy & Environmental Science 15.12 (2022): 5159-5167.

[11] Lee, You-Sun, et al. "High performance direct current-generating triboelectric nanogenerators based on tribovoltaic pn junction with ChCl-passivated CsFAMA perovskite." Nano Energy 106 (2023): 108066.

[12] Li, Hongyun, et al. "High power and low crest factor of direct-current triboelectric nanogenerator for self-powered optical computing system." Energy & Environmental Science 16.10 (2023): 4641-4649.

[13] Zeng, Qixuan, et al. "A Dual-Functional Triboelectric Nanogenerator Based on the Comprehensive Integration and Synergetic Utilization of Triboelectrification, Electrostatic Induction, and Electrostatic Discharge to Achieve Alternating Current/Direct Current Convertible Outputs." Advanced Materials 35.7 (2023): 2208139.

[14] Fan, Beibei, et al. "A wearable DC tribovoltaic power textile woven by P/N-type organic semiconductor fibers." Energy & Environmental Science 17.22 (2024): 8621-8632.
[15] Luo, Jianjun, et al. "Direct-current triboelectric nanogenerator realized by air breakdown induced ionized air channel." Advanced Energy Materials 8.27 (2018): 1800889.
[16] Gao, Yikui, et al. "Spontaneously established reverse electric field to enhance the performance of triboelectric nanogenerators via improving Coulombic efficiency." Nature Communications 15.1 (2024): 4167.
[17] Zhang, Liqiang, et al. "Macro-superlubric triboelectric nanogenerator based on tribovoltaic effect." Matter 5.5 (2022): 1532-1546.
[18] Rahman, Muhammad Toyabur, et al. "Bimetallic nanoporous carbon-based direct-current triboelectric nanogenerators for biomechanical energy harvesting and sensing." Chemical Engineering Journal (2025): 164938.
[19] Yoon, Hong-Joon, et al. "Microdischarge-based direct current triboelectric nanogenerator via accumulation of triboelectric charge in atmospheric condition." Advanced Energy Materials 10.25 (2020): 2000730.
[20] Zhang, Xiankun, et al. "All-van-der-Waals barrier-free contacts for high-mobility transistors." Advanced Materials 34.34 (2022): 2109521.
[21] Li, Qianying, et al. "Overall performance improvement of direct-current triboelectric nanogenerators by charge leakage and ternary dielectric evaluation." Energy & Environmental Science 16.8 (2023): 3514-3525.